Electrochimica Acta 266 (2018) 178–184

Contents lists available at ScienceDirect

Electrochimica Acta

journal homepage: www.elsevier.com/locate/electacta

# Significantly improved performance of red phosphorus sodium-ion anodes with the addition of iron

Li-Chu Chin, Yuan-Hsing Yi, Wei-Chung Chang, Hsing-Yu Tuan*

*Department of Chemical Engineering, National Tsing Hua University, Hsinchu 300, Taiwan, ROC*

## ARTICLE INFO

*Article history:*
Received 25 August 2017
Received in revised form
15 December 2017
Accepted 15 December 2017
Available online 21 December 2017

*Keywords:*
Sodium ion battery
Iron-red phosphorus composites
Rate performance
EIS test

## ABSTRACT

Sodium-ion battery is the most promising alternative to lithium-ion battery for the similar chemical properties to lithium and low cost due to the earth abundance of sodium. Red phosphorus (RP) is regarded as a potential candidate for sodium-ion batteries because it has the highest theoretical capacity (~2600 mA h/g), but commercially available RP is electrochemical inactivity with sodium as a result of the insulating nature. Among the P-based anodes for SIBs, they were all in the form of carbon–P composites. Herein, we report that commercial RP mixed with appropriate amount of iron developed by high-energy ball milling can deliver a reversible capacity of 1642 mA h $g^{-1}$ over 30 cycles. EIS measurement results indicated that Fe content composites has higher sodium diffusion coefficient. When utilized as a sodium ion battery anode, 9.1% Fe-adding RP composites exhibited the best electrochemical performance achieved 1582, 1419, 884 and 676 mA h $g^{-1}$ specific desodiation capacity at 0.2, 0.6, 1, 6 and 10 A $g^{-1}$ current density in rate capability tests. This study opens a new approach to activate the sodium-ion storage of phosphorus, which will enable phosphorus-related materials to be used in more innovative energy storage systems.

## 1. Introduction

Lithium-ion batteries (LIBs) have been successfully utilized as energy storage devices for portable electronics such as mobile phones and lap-top computers for several decades due to their excellent electrochemical performance [1–3]. With the electric car, large energy storage grid and other large battery development, it is expected that the cost of LIBs will dramatically boost in the foreseeable future [4,5]. Therefore, alternative energy storage systems with low cost will be crucially exploited for future applications. Sodium ion batteries (SIBs) have received renewed interest and been considered as a potential alternative to LIBs owing to their abundant natural resources, their lower price of sodium, and the similar chemistry of sodium and lithium [6–8]. In the view of the outstanding experience with carbon anodes in lithium ion batteries (LIBs), carbonaceous materials, such as carbon nanospheres [9], hard carbons [10–12], graphene [13,14] and nanowires [15], have been reported as anode materials for SIBs, but their specific capacities are still relatively low (200–372 mA h $g^{-1}$). In addition to the larger radius of the sodium ion (0.102 nm vs. 0.076 nm) and stretched C–C bond induced by sodiation [15,16], the main difficulty in anode part of sodium-ion batteries is that the most common graphite anode applied in lithium-ion batteries cannot intercalate with sodium ions thermodynamically [17]. Recently, anode materials for sodium-ion batteries that have been studied such as metal oxides ($NiCo_2O_4$, $TiO_2$, $Li_4\ Ti_5O_{12}$ and $Na_2Ti_3O_7$) [18–21], alloys (Sn, Sb, SnSb/C, Sb/C, and $Cu_2Sb$) [22–26], two-dimensional compounds ($MoS_2$/C, MXene/C) [27,28], and carbonaceous materials (hard carbon and doped carbon) [29,30]. However, the specific capacity of these materials is still low (less than 1000 mA h $g^{-1}$) and the cycling life is poor.

Phosphorus (P) is an attractive anode material, which can give the highest theoretical specific capacity of 2596 mA h $g^{-1}$ among all materials for SIBs when $Na_3P$ phase is form. There are three common phosphorus allotrope: white phosphorus, red phosphorus (RP), black phosphorus. White phosphorus is the most reactive, fire spontaneously at room temperature, not suitable as anode material and synthesis of black phosphorus is not facile, which is made from red phosphorus by high temperature and pressure [31]. Compared to the two major forms, red phosphorus is commercially available, environmental benignity and chemically stable [32,33]. However, the application of RP in SIBs is handicapped by its low electrical

---

* Corresponding author.
*E-mail address:* hytuan@che.nthu.edu.tw (H.-Y. Tuan).

https://doi.org/10.1016/j.electacta.2017.12.105

conductivity (~$10^{-12}$ S/m) and large volume expansion (>300%) [34] during sodiation–desodiation process. To address these two drawbacks, RP was often mixed with carbon by high-energy mechanical ball milling to form amorphous P-carbon composites [9,35–39]. In 2013, Qian et al. [9] and Kim et al. [38] have introduced that commercially RP with 30 wt% carbon content produced by high-energy mechanical milling could exhibit a high capacity (~1750 mA h g$^{-1}$) at the current density of 250 mA g$^{-1}$ and a reversible capacity (~1900 mA h g$^{-1}$ at 143 mA g$^{-1}$), respectively. The commercial RP with carbon delivers a large initial specific capacity but cannot react with Na reversibly. Wang et al. [36,37] presented a chemically bonded RP/graphene (7:3, weight ratio) hybrid with stable electrochemical performance 1700 mA h gp$^{-1}$ after 60 cycles and a red phosphorus–carbon nanotube (RP–CNT) anode by chemical bonding between an RP–CNT hybrid and a cross-linked polymer binder with improved cycling retention (1586 mA h g$^{-1}$ after 100 cycles). Dou et al. [40] reported that simply mixing RP–multiwall carbon nanotube (MWCNT) composite displayed a high initial capacity of 1530 mA h gp$^{-1}$ but decayed to 750 mA h gp$^{-1}$ after only 20 cycles. Despite important role of carbon in maintaining electrode conductivity, a high proportion (30%) of the low capacity carbon will sacrifice real battery energy density.

In this work, transition metal "iron" serve as the conductive network and unexpectedly achieve highly reversible sodium storage in commercially available RP. Herein, RP and iron are facilely synthesized with different iron weight percentage 6.3%, 9.1%, 16.6% Fe-RP composites through mechanical ball milling. Evidence of EIS measurement can be found that Fe appeared as a powerful aid as it benefits a higher sodium diffusion coefficient. The significantly increased electronic conductivity combined the higher sodium diffusion coefficient leads to a noticeable enhancement in rate performance and high reversible capacity for the Fe-RP composites. The 9.1% Fe-RP composites showed the best performance exhibits an initial reversible capacity of 1642 mA h g$^{-1}$ for sodium ion storage and ran after 30 cycles, which indicates a significant improvement compared to ref. [38] and a superior performance/cost ratio than previous reports on P carbon-based SIB anodes.

## 2. Experimental section

### 2.1. Materials

Red phosphorus powder (98.9%) were purchased from Alfa Aesar. Poly (acrylic acid) (PAA, average $M_V$ ~3000000), iron powder (98.9%) and ethanol ($C_2H_5OH$, 99.8%) were purchased from Sigma-Aldrich. Sodium hexafluorophosphate ($NaPF_6$), fluoroethylene carbonate (FEC, $C_3H_3FO_3$), diethyl carbonate (DEC, $C_5H_{10}O_3$), Ethylene carbonate (EC, $C_3H_4O_3$), carbon black, sodium metal foil, copper metal foil, and coin-type cell CR2032 were purchased from Shining Energy Co., Ltd. Glass fiber (19 mm) were purchased from Toyo Roshi Kaisha, Ltd.

### 2.2. Fe-RP composites synthesis

First, the Fe-RP composites was synthesized by ball milling of Commercial RP and iron with weight mass ratio of 10:1. The 10 mm stainless steel milling balls and reagent powders was placed into a 50 ml steel jar which taken to argon-filled glovebox and sealed under argon atmosphere, followed by ball-milling for 2 h at a speed of 200 rpm. For comparisons, red phosphorus powders were prepared by the same ball-milling for 2 h without iron (denoted as RP).

### 2.3. Sodium -ion battery assembly and electrochemical characterization

50 wt % active materials (Fe-RP composites), 25 wt % carbon black, 25 wt % PAA were mixed in ethanol to form a homogeneous slurry, using stir bar to dissolved all material in ethanol, keeping stirring for 12 h or longer till all material were well-dispersed in ethanol. The slurry was tape-casted on a copper foil and dried at room temperature to fabricate the electrode of phosphorus. Before assembled, the electrode was dried at 150 °C for 30 min under argon atmosphere to remove the residual water. The coin-typed half-cell (CR2032), which contained a Fe-RP composites electrode, a sodium metal as the counter electrode and a glass fiber soaked in an electrolyte, was assembled in an argon-filled glovebox. The electrolyte was consisted of 1 M $NaPF_6$ in a mixture of fluoroethylene carbonate/diethyl carbonate (PC: DMC: FEC) (5:5:1 v/v). The electrochemical performance of the half-cell was tested by using Maccor Series 4000 at the voltage range between 0.01 V and 2.0 V. Average mass of active materials on the copper foil is approximately 0.5 mg/cm$^2$ for half-cell.

### 2.4. Characterization

The structural investigations of Fe-RP composites were carried out by using scanning electron microscopy (HITACHI-SU8010) with energy-dispersive X-ray spectroscopy (HORIBA, EX-250), transmission electron microscopy (TECNAI 20), X-ray diffraction (Rigaku Ultima IV), Raman spectroscopy (LABRAM HR 800 UV) with a radiation of 532 nm. X-ray photoelectron spectroscopy (XPS) measurements were obtained by using PHI 5000 Versaprobe II. The TEM samples were prepared by dispersing the powder in the ethanol and drop-casting onto a copper grid. XRD pattern were recorded by a Shimadzu XRD-6000 diffractometer, which was equipped with CuK radiation.

## 3. Result and discussion

Fe-RP composites with high phosphorus content 90% could be facilely synthesized by ball milling in the condition of argon atmosphere, as shown in Scheme 1. The RP and iron used in this work are both commercially available, and their morphologies before ball milling are shown in Fig. S1, representing a facile, time saving (only 2 h) and low energy consumption fabrication process compared to previous studies. Fig. 1 shows the XRD patterns and Raman spectra for commercial RP, iron powder (Fe), and weight percentage 6.3%, 9.1%,16.6% Fe-RP composites (denoted as 6.3%, 9.1%,16.6% Fe-RP). The XRD pattern (Fig. 1(a)) of the commercial RP shows a sharp diffraction peak at 15°, 35°, consistent with the XRD pattern of commercial RP reported in the literature [9,34]. The main diffraction peaks of iron powder (Fe) is identical, which can be well indexed to Fe phase (JCPDS no. 87-0722) with a space group of Im-

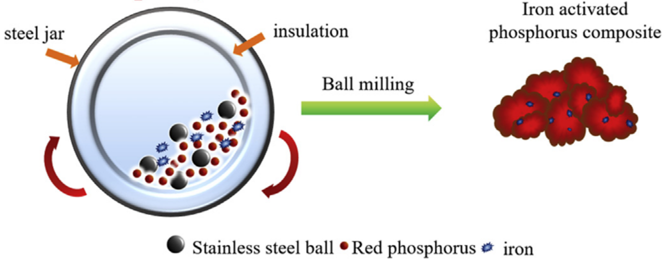

**Scheme 1.** Schematic illustration of the preparation of Fe-RP composites.

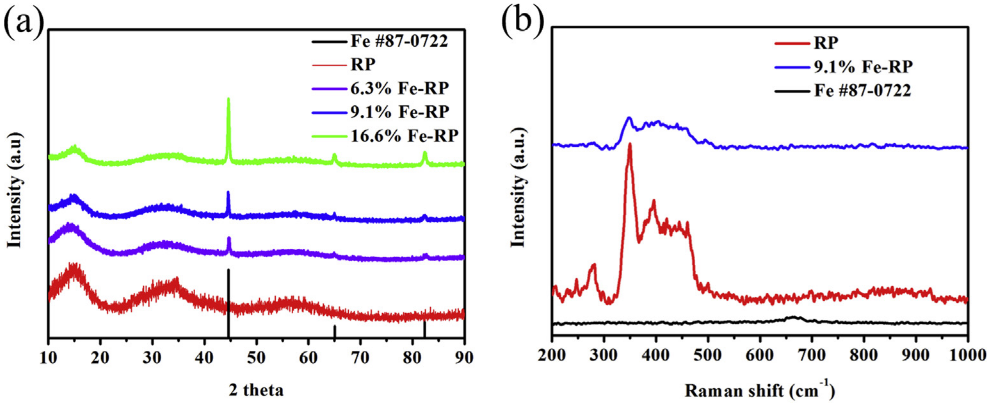

**Fig. 1.** (a) XRD patterns for RP, 6.3%Fe-RP, 9.1% Fe-RP and 16.6% Fe-RP (b) Raman spectra for RP and 9.1% Fe-RP.

3m (229). Owing to shorter ball milling time (2 h), remained both of their origin structure and no more peaks are found for 6.3%, 9.1%,16.6% Fe-RP except those of iron and red P, indicating no interaction or bonding formed between red P and iron. Apart from pure red phosphorus, 6.3%, 9.1%,16.6% Fe-RP electrode shows characteristic crystalline peaks indicating the lattice planes of iron at 44.6°, 65.1° and 82.3°, which explained Fe still remain its crystalline phase. Different from previous amorphousizing RP/carbon based anodes [9,32,36,41,42], this is the RP mixed iron composites with extraordinarily high capacity, and considerable high rate capability, as a novel anode material for sodium ion batteries. Besides, the Raman spectrum (Fig. 1(b)) attained for 9.1% Fe-RP was similar to the spectrum of commercial RP with the presence of three bands between 300 and 500 cm$^{-1}$ [43]. In addition, the Raman peaks of 9.1% Fe-RP were a little weaker when compared to those of RP, which could be likely due to the facts that particle size of RP was reduced to microsizes [44].

Observed from SEM images, the particle size of both bulk commercial RP and iron (Fig. S1) was broken down to featureless agglomerated particles with diameter around 0.5–1 µm after ball milling (Fig. 2(a–b)). In order to confirm the elemental compositions of Fe-RP composites, energy-dispersive X-ray spectroscopy (EDS) (Fig. 2(c)) was carried out. The EDS spectra shows that Fe-RP composites is almost composed of elemental phosphorus with little iron appeared at around 6.4 keV. The low magnification TEM image in (Fig. 2 d) confirmed that the particles of Fe-RP composites have a particle size of about 0.5 µm. The high-magnification TEM image of the Fe-RP composites (Fig. 2(e)) shows a clear fringe. Indeed, after ball milling the particle size only submicron to a few microns, much smaller than those of the bulk phosphorus, as shown in Fig. S2(a). Elemental mapping analysis of Fe-RP composites (Fig. 2(d–g)) confirms the homogeneous distribution of P and Fe elements in the particle. Moreover, the decreased particle size after ball milling could dramatically decrease the diffusion length of Na$^{+}$ and e$^{-}$, resulting in extraordinarily improved kinetics of sodium ions transferring and appropriate amount of Fe adding would be helpful

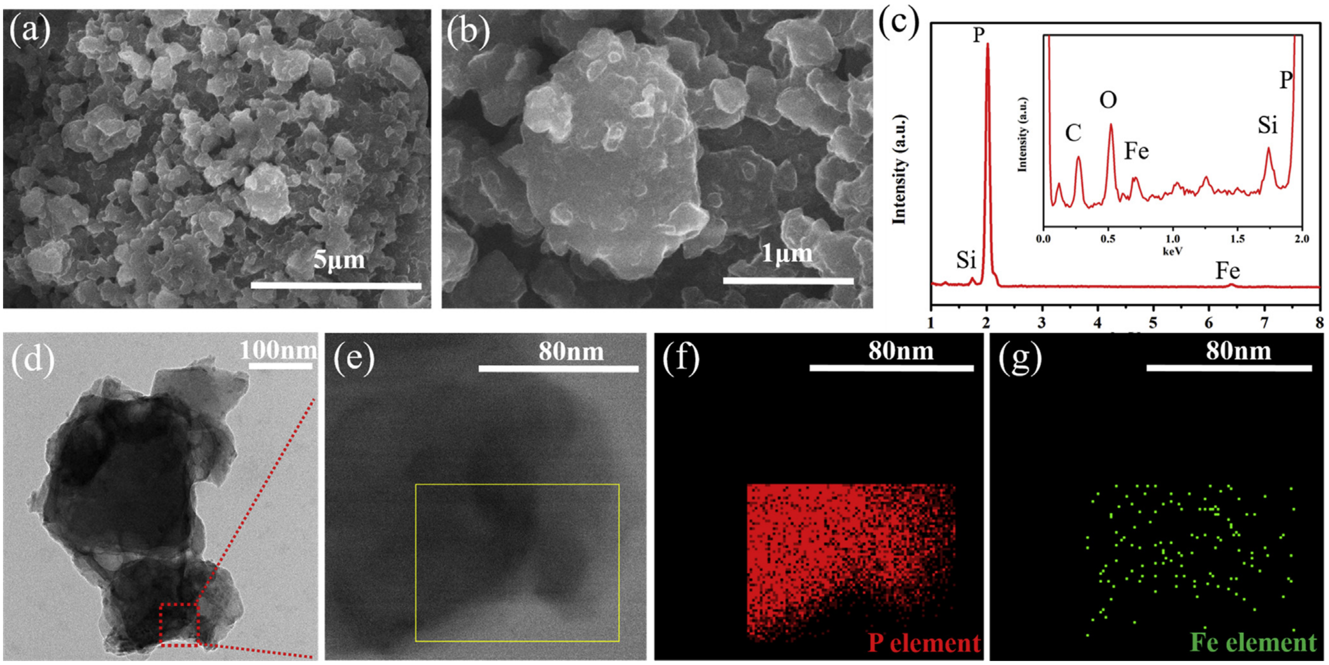

**Fig. 2.** (a, b) SEM images of Fe-RP composites by milling for 2 h at a speed of 200 rpm (c) EDS spectra of Fe-RP composites. The inset image is the magnification. (d) Low and (e) high magnification TEM images (f, g) elemental mapping of RP-Fe composites (f) phosphorus (red) and (g) iron (green). (For interpretation of the references to colour in this figure legend, the reader is referred to the Web version of this article.)

for increasing the electronic conductivity of the red phosphorus.

To further investigate the interaction between RP and iron, X-ray photoelectron spectroscopy (XPS) was applied to analyze the surface chemical compositions of the samples in Fig. 3(a–d). The survey spectra in Fig. 3(a) show similar peaks of P, C and O elements except for an obvious Fe 2p peak in 9.1% Fe-RP, confirming the iron contain. A high resolution XPS spectrum of RP in Fig. 3(b) shows two distinct P $2p_{1/2}$ and P $2p_{3/2}$ peaks at 129.1 eV and 130.0 eV, respectively. Broad peaks at a higher energy range are also observed at 133.6 eV, which can be assigned to the P—O bond [43]. Comparing the XPS spectra of Fe-RP composites, higher intensity of P—O bond indicates that more oxygen/oxidation exists in Fe-RP composites surface which is indicative of iron easy to oxidize when exposed to air [45]. The Fe 2p XPS peaks at 711.1 and 723.4 eV are attributed to Fe $2p_{3/2}$ and Fe $2p_{1/2}$, confirming the existence of oxidized Fe (III) and Fe (II) [46,47]. This suggests that the iron are in intimate contact with phosphorus and mainly located on the surface of the phosphorus particles.

The electrochemical performance of the Fe-RP composites was tested by coin-typed half-cell (CR2032) within the range between 0.01 V and 2.0 V. Unless stated, all of the capacity was calculated on the basis of the mass of composites in this study. Electrodes composed of Fe-RP composites, carbon black, and binder (poly acrylic acid) (50:25:25, weight ratio) were used as working electrodes, and sodium was used as counter electrodes. Fig. 4(a) shows the cycling performance of RP, 6.3%, 9.1%, 16.6%Fe-RP composites at rate of 0.4 A/g. RP has a desodiation capacity 1900 mA h/$g_{composite}$ in the first cycle but decreases to below 423 mA h/$g_{composite}$ after only 20 cycles (Fig. 4(a)). Although iron is beneficial to improve the conductivity of the whole composite, it could be hinder reaction between sodium ion and phosphorus with excess adding (16.3%) due to its intrinsically inactive to sodium. Obviously, Fe-RP composites with 9.1% iron addition displayed outstanding reversible capacity performance, it still maintains a reversible capacity of 1270 mA h/$g_{composite}$ after 30 cycles. The initial columbic efficiency of 9.1% Fe-RP (78.8%) is better than RP (68%) and achieves above 96% after second cycle, the irreversible capacity was mainly caused by forming a SEI layer on the electrode during the first discharge and charge processes. Galvanostatic charge/discharge curves of the 9.1% Fe-RP at a current density of 400 mA/$g_{composite}$ in the voltage range of 0.01–2 V are displayed in Fig. 4(b). In Fig. 4(b) exhibit several potential plateaus, which are observed in the first discharge (sodiation) process at 0.74–0.8 V, 0.1–0.4 V and in the first charge (desodiation) process at 0.6–0.65 V. In the following cycles, the plateaus can be observed at 0.25–0.4 V in the discharge process and at 0.6–0.65 V in the charge process. Fig. 4(c) show the differential capacity curves at various cycles, including the 1st, 5th and 30th cycle. The peaks indicate the sodiation and desodiation of the composites. In the first discharge cycle, the sharp peak appeared at 0.76–0.81 V corresponding to the electrochemical decomposition of electrolyte for the formation of a solid-electrolyte interface (SEI) film on the electrode surface. The rest of peaks at the first discharge cycle at 0.1 V–0.4 V are the formation of $Na_3P$ and $Na_xP$, respectively [38]. In the first charge cycle, a stepwise sodium ion deintercalation from the fully charged $Na_3P$ phases to form the $Na_2P$, NaP, and $NaP_7$ intermediates were appeared at 0.6–0.65 V based on the Na/P phase diagram [36,38]. All the differential capacity curves matched well with the voltage plateaus in the charge/discharge curves in Fig. 4(b) and stayed almost unchanged in subsequent cycles, indicating quite reversible sodium–phosphorus insertion/extraction reactions. In order to investigate the effect of Fe-adding on the electrode kinetics of red phosphorus, electrochemical impedance spectroscopy was employed to compare the diffusion coefficient of sodium ions of electrode materials. Fig. 4(d)

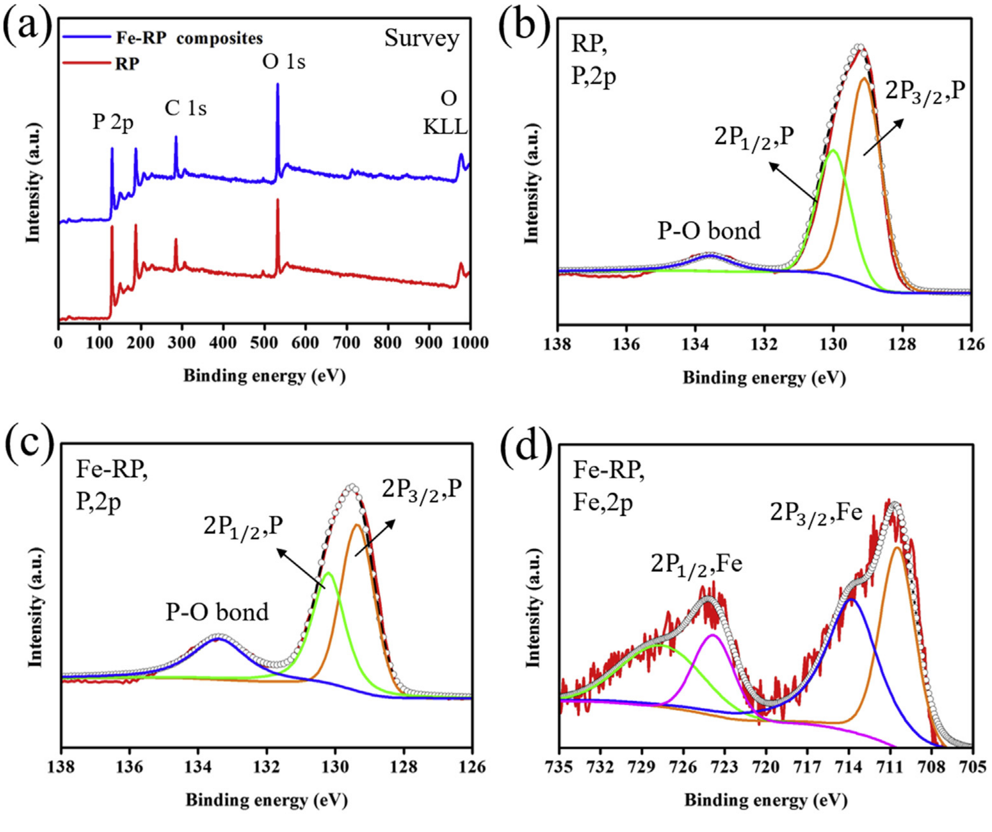

**Fig. 3.** (a) XPS survey, (b) (c) P 2p spectra of RP and Fe-RP composites. (d) Fe 2p spectrum of Fe-RP composites.

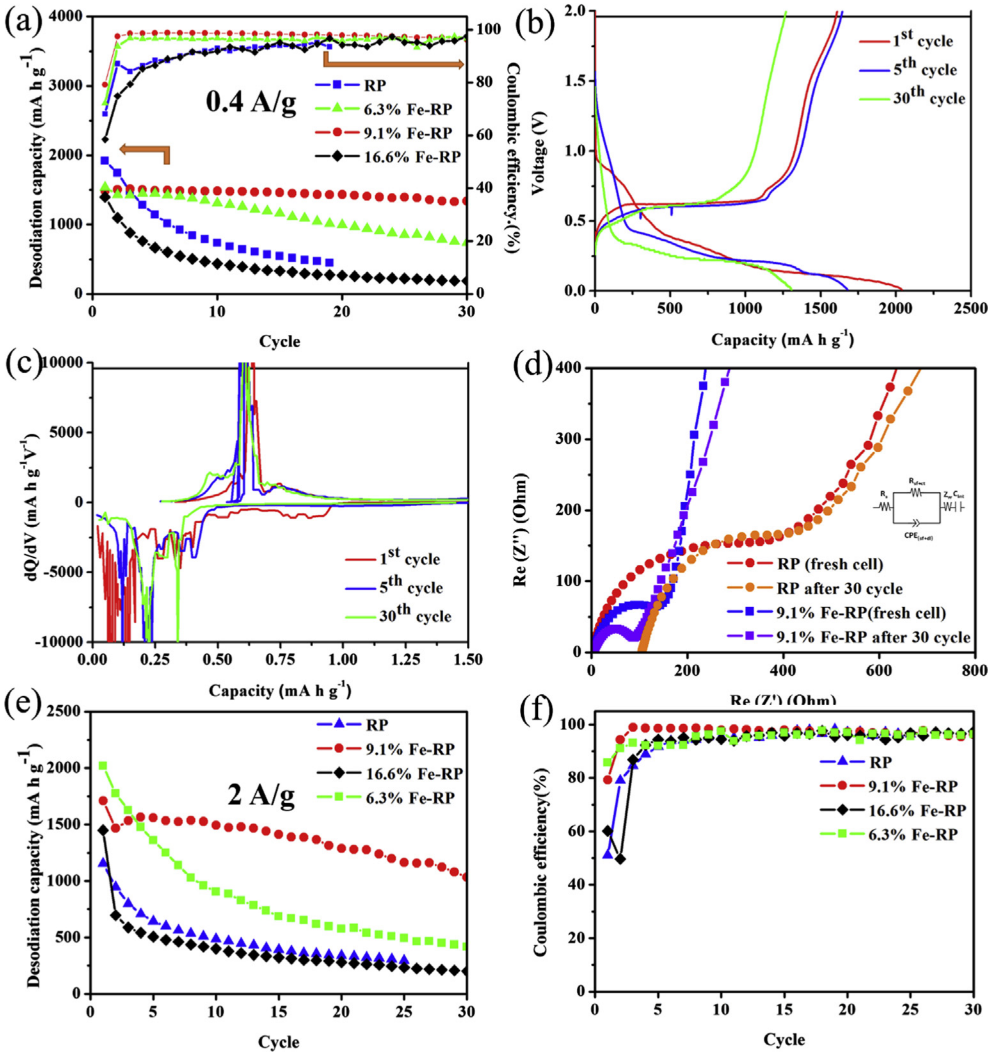

**Fig. 4.** (a) Cycling performance of the RP 6.3%Fe-RP, 9.1% Fe-RP and 16.6% Fe-RP at a rate of 0.4 A/g. and (b) Charge-discharge voltage profiles of 9.1% Fe-RP at 1st, 5th and 30th cycles. (c) Differential capacity curves of the 9.1% Fe-RP at 1st, 5th and 30th cycles. (d) EIS plots of the RP (fresh cell) and 9.1% Fe-RP (fresh cell and after 30 cycle) at a full charge state. (e) Cycling performance and (f) Coulombic efficiency of the RP, 6.3% Fe-RP, 9.1% Fe-RP,16.6% Fe-RP electrode at a current density of 0.2 A/g for activation and then at 2 A/g in the subsequent cycles.

shows a comparison of electrochemical impedance spectroscopy (EIS) between the ball-milled RP (fresh cell) we used and 9.1% phosphorus composite (fresh cell and after 30 cycles) with a full charge state at 2 A rate. The Nyquist plot comprises a semicircle at medium frequency region and a straight line at low frequency region, were illustrated by electric equivalent circuit displayed in the inset of Fig. 4(d). As frequency decreases, there is a semicircle called charge transfer resistance, indicating that sodium ions passing through the SEI film and charge transfer between electrolyte and active material [48]. The 9.1% Fe-RP electrode showed the smaller diameter of the semicircle with fresh cell, which explains that the RP electrodes possess the larger charge transfer resistance. Charge transfer resistance decreased from 400 to 187 Ω after ball milling iron, indicating electrode structure transformation favorable to electron transfer and sodium ion diffusion in the electrode during cycling [49]. The 9.1% Fe-RP electrode showed the smaller diameter of the semicircle after 30 cycles, which suggests that the fresh electrodes possess the larger charge transfer resistance. Besides, the sloping region is Warburg impedance accounting for diffusion resistance of the electrolyte ions into the electrode. The slope decreased at the low frequency region after 30 cycles, implying a decreased diffusion resistance due to generation of facile sodium diffusion channels. This result is in good agreement with rates cycle performance measurement results.

To explore the optimized ratio of iron and RP, 6.3%, 9.1%, 16.6% Fe-RP composites were tested at a current density of 0.2 A/g at the first cycle for activation and then switched to a higher current density of 2 A/g in the subsequent cycles. A higher RP/Fe ratio is beneficial in terms of specific capacity, given that iron is electrochemically inactive for sodiation. Therefore, 16.6% Fe-RP composites has lower desodiation capacity than RP due to a lot of inactive iron containing. In Fig. 4(e), compared to 9.1% Fe-RP, 6.3% Fe-RP deliver a faster capacity decrease and a poorer cycling stability. In this study, the 9.1% Fe-RP electrode exhibits the best cycling stability than the other electrodes. It still maintains a reversible capacity of 1033 mA h/g$_{composite}$ after 30 cycles, which proved that given suitable iron can provide a stable desodiation capacity. Hence, the following electrochemical characterization was carried out on the optimized 9.1% Fe-RP. Fig. 4(f) shows the coulombic efficiency of different materials corresponding to Fig. 4(e). The first cycle coulombic efficiency of RP is the lowest one among them (~50%). With the iron added, the first cycle of 9.1% Fe-RP and 6.3%

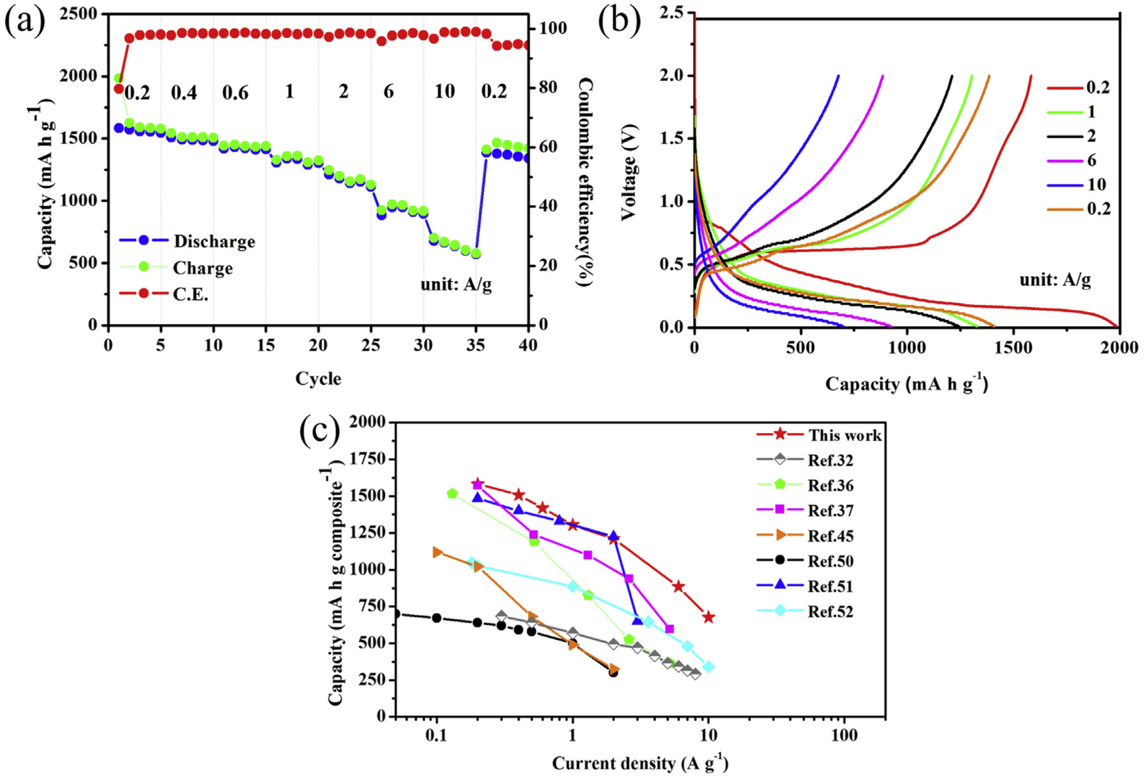

**Fig. 5.** Rate capability of the 9.1% Fe-RP from 0.2 to 10 A/g. (a) all of the discharge rates are equal to the charge rates. (b) Voltage profiles of 9.1% Fe-RP at different current densities. (c) Rate capability of this study is comparable with those of previous studies about nanoparticle-decorated, carbon nanotube-based, carbon-based phosphorus and graphene-based RP. The red star symbolizes our data, which were calculated based on the whole composites, from 0.2 to 10 A/g (discharge and charge rates were kept the same). (For interpretation of the references to colour in this figure legend, the reader is referred to the Web version of this article.)

Fe-RP coulombic efficiency increases to ~80% probably due to the moderately improved conductivity by iron. The coulombic efficiency of the 9.1% Fe-RP exceeds 94% after the second cycle, and remains stable during the rest of cycles. We thought that appropriate amount of iron served as an activator to improve rate performance and high reversible capacity and the optimize ratio of iron is 9.1% in our study.

To be consistent with practical situation, we also evaluated the rate performance of the anode using the 9.1% Fe-RP with current densities ranging from 0.2 to 10 A/g, as shown in Fig. 5(a) and the corresponding sodiation desodiation curves plotted in Fig. 5(b). As the current density increased, a specific capacity of 1582 (0.2 A/g), 1507 (0.4 A/g), 1419 (0.6 A/g), 1304 (1 A/g), 1210 (2 A/g), 884 (6 A/g), 676 (10 A/g), and 1385 (0.2 A/g) mA h/g, respectively. Even at 10 A/g, the composites anode still can deliver a high reversible capacity of ~676 mA h/g. When the rate was restored to 200 mA/g after 40 cycles of rate testing, the specific capacity of the 9.1% Fe-RP anode returned to 1385 mA h/g is nearly equivalent to initially average capacity (1582 mA h/g) from the initial 200 mA/g trial. This indicates that the anode charge/discharge was reversible even at high current density.

The electrochemical performance of 9.1% Fe-RP is compared with that of some previously reported SIB anodes and plotted in Fig. 5(c). 9.1% Fe-RP shows the superior rate capability from 0.2 A/g to 10 A/g (discharge and charge rates were kept the same) in comparison with those based on graphene-based RP [36], carbon nanotube-based RP [37,50,51], and carbon-based phosphorus [32,45,52]. These data explain well that the 9.1% Fe-RP is very competitive, not only in capacity output, but also high rate capability. In this work, the superior high rate capability can be ascribed to stable solid electrolyte interphase and ultra-fast electrode transport due to the intimate contact between RP and iron, such a unique crystalline nature of iron could greatly enhance the electronic conductivity, increase the mechanical strength of the composite, and hence improve its rate performance.

## 4. Conclusion

In summary, Fe-RP composites had been successfully synthesized through a facile ball milling method and RP were embedded by Fe particles. The Fe-RP composites can be cycled reversibly with little iron content (<10%), not only ensuring the real battery energy density but also deliver the superior reversible capacity and rate capability. Iron plays a crucial role in the reversibility of the Fe-RP composites, which provides pathways for electron transport. However, the critical mechanism of iron's capacity reversible still remains unknown, which is a very interesting issue for further study. Our results open a new milestone for the activation of phosphorus, which will enable phosphorus-related materials to be used in more innovative energy storage systems.

## Acknowledgment

We acknowledge the financial support by the Ministry of Science and Technology of Taiwan through the grants of MOST 106-2628-E-007-005-MY3, MOST 103-2221-E-007-089-MY3, MOST 106-2221-E-007 -081 -MY3, and MOST 105-2622-8-007-009.

## Appendix A. Supplementary data

Supplementary data related to this article can be found at https://doi.org/10.1016/j.electacta.2017.12.105.

## References

[1] B.L. Ellis, K.T. Lee, L.F. Nazar, Positive electrode materials for Li-ion and Li-batteries, Chem. Mater. 22 (2010) 691–714.

[2] P.G. Bruce, B. Scrosati, J.M. Tarascon, Nanomaterials for rechargeable lithium batteries, Angew. Chem. Int. Ed. 47 (2008) 2930–2946.

[3] U. Kasavajjula, C. Wang, A.J. Appleby, Nano-and bulk-silicon-based insertion anodes for lithium-ion secondary cells, J. Power Sources 163 (2007) 1003–1039.

[4] B. Dunn, H. Kamath, J.-M. Tarascon, Electrical energy storage for the grid: a battery of choices, Science 334 (2011) 928–935.

[5] M.D. Slater, D. Kim, E. Lee, C.S. Johnson, Sodium-ion batteries, Adv. Funct. Mater. 23 (2013) 947–958.

[6] V. Palomares, P. Serras, I. Villaluenga, K.B. Hueso, J. Carretero-González, T. Rojo, Na-ion batteries, recent advances and present challenges to become low cost energy storage systems, Energy Environ. Sci. 5 (2012) 5884–5901.

[7] S.W. Kim, D.H. Seo, X. Ma, G. Ceder, K. Kang, Electrode materials for rechargeable sodium-ion batteries: potential alternatives to current lithium-ion batteries, Adv. Energy Mater. 2 (2012) 710–721.

[8] N. Yabuuchi, K. Kubota, M. Dahbi, S. Komaba, Research development on sodium-ion batteries, Chem. Rev. 114 (2014) 11636–11682.

[9] J. Qian, X. Wu, Y. Cao, X. Ai, H. Yang, High capacity and rate capability of amorphous phosphorus for sodium ion batteries, Angew. Chem. 125 (2013) 4731–4734.

[10] R. Alcántara, J.J. Mateos, J. Tirado, Negative electrodes for lithium-and sodium-ion batteries obtained by heat-treatment of petroleum cokes below 1000 C, J. Electrochem. Soc. 149 (2002) A201–A205.

[11] D. Stevens, J. Dahn, High capacity anode materials for rechargeable sodium-ion batteries, J. Electrochem. Soc. 147 (2000) 1271–1273.

[12] S. Komaba, W. Murata, T. Ishikawa, N. Yabuuchi, T. Ozeki, T. Nakayama, A. Ogata, K. Gotoh, K. Fujiwara, Electrochemical Na insertion and solid electrolyte interphase for hard-carbon electrodes and application to Na-Ion batteries, Adv. Funct. Mater. 21 (2011) 3859–3867.

[13] Y.-X. Wang, S.-L. Chou, H.-K. Liu, S.-X. Dou, Reduced graphene oxide with superior cycling stability and rate capability for sodium storage, Carbon 57 (2013) 202–208.

[14] Z. Yu, J. Song, M.L. Gordin, R. Yi, D. Tang, D. Wang, Phosphorus-graphene nanosheet hybrids as lithium-ion anode with exceptional high-temperature cycling stability, Adv. Syst. 2 (2015).

[15] Y. Cao, L. Xiao, M.L. Sushko, W. Wang, B. Schwenzer, J. Xiao, Z. Nie, L.V. Saraf, Z. Yang, J. Liu, Sodium ion insertion in hollow carbon nanowires for battery applications, Nano Lett. 12 (2012) 3783–3787.

[16] P. Ge, M. Fouletier, Electrochemical intercalation of sodium in graphite, Solid State Ionics 28 (1988) 1172–1175.

[17] D. Kundu, E. Talaie, V. Duffort, L.F. Nazar, The emerging chemistry of sodium ion batteries for electrochemical energy storage, Angew. Chem. Int. Ed. 54 (2015) 3431–3448.

[18] D. Wu, X. Li, B. Xu, N. Twu, L. Liu, G. Ceder, NaTiO 2: a layered anode material for sodium-ion batteries, Energy Environ. Sci. 8 (2015) 195–202.

[19] Y. Sun, L. Zhao, H. Pan, X. Lu, L. Gu, Y.-S. Hu, H. Li, M. Armand, Y. Ikuhara, L. Chen, Direct atomic-scale confirmation of three-phase storage mechanism in Li4Ti5O12 anodes for room-temperature sodium-ion batteries, Nat. Commun. 4 (2013) 1870.

[20] P. Senguttuvan, G. Rousse, V. Seznec, J.-M. Tarascon, M.R. Palacin, Na2Ti3O7: lowest voltage ever reported oxide insertion electrode for sodium ion batteries, Chem. Mater. 23 (2011) 4109–4111.

[21] H. Xiong, M.D. Slater, M. Balasubramanian, C.S. Johnson, T. Rajh, Amorphous TiO2 nanotube anode for rechargeable sodium ion batteries, J. Phys. Chem. Lett. 2 (2011) 2560–2565.

[22] Y. Xu, Y. Zhu, Y. Liu, C. Wang, Electrochemical performance of porous carbon/tin composite anodes for sodium-ion and lithium-ion batteries, Adv. Energy Mater. 3 (2013) 128–133.

[23] S. Liu, J. Feng, X. Bian, J. Liu, H. Xu, The morphology-controlled synthesis of a nanoporous-antimony anode for high-performance sodium-ion batteries, Energy Environ. Sci. 9 (2016) 1229–1236.

[24] L. Xiao, Y. Cao, J. Xiao, W. Wang, L. Kovarik, Z. Nie, J. Liu, High capacity, reversible alloying reactions in SnSb/C nanocomposites for Na-ion battery applications, Chem. Commun. 48 (2012) 3321–3323.

[25] J. Qian, Y. Chen, L. Wu, Y. Cao, X. Ai, H. Yang, High capacity Na-storage and superior cyclability of nanocomposite Sb/C anode for Na-ion batteries, Chem. Commun. 48 (2012) 7070–7072.

[26] L. Baggetto, E. Allcorn, A. Manthiram, G.M. Veith, Cu 2 Sb thin films as anode for Na-ion batteries, Electrochem. Commun. 27 (2013) 168–171.

[27] C. Zhu, X. Mu, P.A. van Aken, Y. Yu, J. Maier, Single-layered ultrasmall nanoplates of MoS2 embedded in carbon nanofibers with excellent electrochemical performance for lithium and sodium storage, Angew. Chem. Int. Ed. 53 (2014) 2152–2156.

[28] X. Xie, M.-Q. Zhao, B. Anasori, K. Maleski, C.E. Ren, J. Li, B.W. Byles, E. Pomerantseva, G. Wang, Y. Gogotsi, Porous heterostructured MXene/carbon nanotube composite paper with high volumetric capacity for sodium-based energy storage devices, Nano Energy 26 (2016) 513–523.

[29] Y. Li, Y.S. Hu, M.M. Titirici, L. Chen, X. Huang, Hard carbon microtubes made from renewable cotton as high-performance anode material for sodium-ion batteries, Adv. Energy Mater. 6 (2016).

[30] L. Qie, W. Chen, X. Xiong, C. Hu, F. Zou, P. Hu, Y. Huang, Sulfur-doped carbon with enlarged interlayer distance as a high-performance anode material for sodium-ion batteries, Adv. Syst. 2 (2015).

[31] C.M. Park, H.J. Sohn, Black phosphorus and its composite for lithium rechargeable batteries, Adv. Mater. 19 (2007) 2465–2468.

[32] W. Li, S. Hu, X. Luo, Z. Li, X. Sun, M. Li, F. Liu, Y. Yu, Confined amorphous red phosphorus in MOF-derived N-Doped microporous carbon as a superior anode for sodium-ion battery, Adv. Mater. 29 (2017).

[33] C. Zhang, X. Wang, Q. Liang, X. Liu, Q. Weng, J. Liu, Y. Yang, Z. Dai, K. Ding, Y. Bando, Amorphous phosphorus/nitrogen-doped graphene paper for ultra-stable sodium-ion batteries, Nano Lett. 16 (2016) 2054–2060.

[34] N. Yabuuchi, Y. Matsuura, T. Ishikawa, S. Kuze, J.Y. Son, Y.T. Cui, H. Oji, S. Komaba, Phosphorus electrodes in sodium cells: small volume expansion by sodiation and the surface-stabilization mechanism in aprotic solvent, ChemElectroChem 1 (2014) 580–589.

[35] T. Ramireddy, T. Xing, M.M. Rahman, Y. Chen, Q. Dutercq, D. Gunzelmann, A.M. Glushenkov, Phosphorus–carbon nanocomposite anodes for lithium-ion and sodium-ion batteries, J. Mater. Chem. 3 (2015) 5572–5584.

[36] J. Song, Z. Yu, M.L. Gordin, S. Hu, R. Yi, D. Tang, T. Walter, M. Regula, D. Choi, X. Li, Chemically bonded phosphorus/graphene hybrid as a high performance anode for sodium-ion batteries, Nano Lett. 14 (2014) 6329–6335.

[37] J. Song, Z. Yu, M.L. Gordin, X. Li, H. Peng, D. Wang, Advanced sodium ion battery anode constructed via chemical bonding between phosphorus, carbon nanotube, and cross-linked polymer binder, ACS Nano 9 (2015) 11933–11941.

[38] Y. Kim, Y. Park, A. Choi, N.S. Choi, J. Kim, J. Lee, J.H. Ryu, S.M. Oh, K.T. Lee, An amorphous red phosphorus/carbon composite as a promising anode material for sodium ion batteries, Adv. Mater. 25 (2013) 3045–3049.

[39] Z. Yu, J. Song, D. Wang, D. Wang, Advanced anode for sodium-ion battery with promising long cycling stability achieved by tuning phosphorus-carbon nanostructures, Nano Energy 40 (2017) 550–558.

[40] W.J. Li, S.L. Chou, J.Z. Wang, H.K. Liu, S.X. Dou, Simply mixed commercial red phosphorus and carbon nanotube composite with exceptionally reversible sodium-ion storage, Nano Lett. 13 (2013) 5480–5484.

[41] J. Qian, D. Qiao, X. Ai, Y. Cao, H. Yang, Reversible 3-Li storage reactions of amorphous phosphorus as high capacity and cycling-stable anodes for Li-ion batteries, Chem. Commun. 48 (2012) 8931–8933.

[42] W. Li, Z. Yang, M. Li, Y. Jiang, X. Wei, X. Zhong, L. Gu, Y. Yu, Amorphous red phosphorus embedded in highly ordered mesoporous carbon with superior lithium and sodium storage capacity, Nano Lett. 16 (2016) 1546–1553.

[43] W.-C. Chang, K.-W. Tseng, H.-Y. Tuan, Solution synthesis of iodine-doped red phosphorus nanoparticles for lithium-ion battery anodes, Nano Lett. 17 (2017) 1240–1247.

[44] Z. Xu, Y. Zeng, L. Wang, N. Li, C. Chen, C. Li, J. Li, H. Lv, L. Kuang, X. Tian, Nanoconfined phosphorus film coating on interconnected carbon nanotubes as ultrastable anodes for lithium ion batteries, J. Power Sources 356 (2017) 18–26.

[45] B. Peng, Y. Xu, K. Liu, X. Wang, F.M. Mulder, High performance and low cost sodium ion anode Based on A Facile black phosphorus-carbon nanocomposite, ChemElectroChem 4 (2017) 1–6.

[46] H. He, D. Sun, Q. Zhang, F. Fu, Y. Tang, J. Guo, M. Shao, H. Wang, Iron-doped cauliflower-like rutile TiO2 with superior sodium storage properties, ACS Appl. Mater. Interfaces 9 (2017) 6093–6103.

[47] S. Bandyopadhyay, G. Singh, I. Sandvig, A. Sandvig, R. Mathieu, P.A. Kumar, W.R. Glomm, Synthesis and in vitro cellular interactions of superparamagnetic iron nanoparticles with a crystalline gold shell, Appl. Surf. Sci. 316 (2014) 171–178.

[48] A. Jossen, Fundamentals of battery dynamics, J. Power Sources 154 (2006) 530–538.

[49] Y. Sun, X. Hu, W. Luo, F. Xia, Y. Huang, Reconstruction of conformal nanoscale MnO on graphene as a high-capacity and long-life anode material for lithium ion batteries, Adv. Funct. Mater. 23 (2013) 2436–2444.

[50] Y.J. Zhu, Y. Wen, X.L. Fan, T. Gao, F.D. Han, C. Luo, S.C. Liou, C.S. Wang, Red phosphorus single-walled carbon nanotube composite as a superior anode for sodium ion batteries, ACS Nano 9 (2015) 3254–3264.

[51] G.-L. Xu, Z. Chen, G.-M. Zhong, Y. Liu, Y. Yang, T. Ma, Y. Ren, X. Zuo, X.-H. Wu, X. Zhang, Nanostructured black phosphorus/Ketjenblack–multiwalled carbon nanotubes composite as high performance anode material for sodium-ion batteries, Nano Lett. 16 (2016) 3955–3965.

[52] J. Sun, H.-W. Lee, M. Pasta, Y. Sun, W. Liu, Y. Li, H.R. Lee, N. Liu, Y. Cui, Carbothermic reduction synthesis of red phosphorus-filled 3D carbon material as a high-capacity anode for sodium ion batteries, Energy Storage Mater. 4 (2016) 130–136.